Investigations of the microstructural response to a cold forging process of the 6082-T6 alloy

Jérémie Bouquerel, Bandiougou Diawara, André Dubois, Mirentxu Dubar, Jean-Bernard Vogt, Denis Najjar

Materials and Design 68 (2015) 245–258

Contents lists available at ScienceDirect

Materials and Design

journal homepage: www.elsevier.com/locate/matdes

Investigations of the microstructural response to a cold forging process of the 6082-T6 alloy

J. Bouquerel [a], B. Diawara [a,b,c], A. Dubois [b], M. Dubar [b,*], J.-B. Vogt [a], D. Najjar [c]

[a] Université Lille Nord de France, ENSCL, UMET, CNRS, UMR 8207, F-59655 Villeneuve d'Ascq, France
[b] Université Lille Nord de France, UVHC, TEMPo EA 4542, F-59313 Valenciennes, France
[c] Université Lille Nord de France, EC Lille, LML, CNRS, UMR 8107, F-59650 Villeneuve d'Ascq, France

ARTICLE INFO

Article history:
Received 18 November 2013
Accepted 2 December 2014
Available online 9 December 2014

Keywords:
Cold forging
Aluminium alloy
Electron backscatter diffraction
Line segment method
Misorientation parameters

ABSTRACT

The microstructure of 6082 aluminium alloy in artificial aged condition was investigated before and after cold forming. The cold forming process was performed at room temperature with and without lubricant. An in depth microstructure investigation has been carried out through electron backscatter diffraction (EBSD) analysis. Different approaches were considered to quantify the plastic strain: the Line Segment Method (LSM) and the study of misorientations trough the Kernel Average Misorientation (KAM), the Grain Orientation Spread (GOS) and the Grain Average Misorientation (GAM). The evidence of intermetallic particles removal from their location during plastic deformation was observed. Values of plastic strain lower than 0.1 did not affect the grain size itself. Nonetheless it induced the development of sub-structures which may lead to the hardening of the alloy.

1. Introduction

Looking for lightweight components is a challenge of major importance In the transport industry. Indeed, mass reduction is one of the responses to the Kyoto Protocol which aims to tackles the emissions of six greenhouse gases, including the carbon dioxide (CO_2), methane (CH_4), nitrous oxide (N_2O) and some fluoride gases. As most of the forces applied on a vehicle are proportional to its weight, a reduction in mass implies a reduction of the driving force and consequently a reduction in energy consumption. Moreover a light car is also safer since it possesses a smaller inertia and will require a shorter distance to stop than a heavy car. Getting mass reduction of the vehicles is closely related to the use of light materials such as aluminium alloys [1,2]. The 6xxx alloys have been extensively studied because of their technical importance and their exceptional increase in strength obtained by precipitation hardening. They are also largely used in automotive and aeronautic components because of their impact on weight reduction.

Those alloys contain magnesium and silicon as major addition elements, which are partly dissolved in the primary α-Al matrix, and partly present in the form of intermetallic phase [3–6]. Fe is also present as an impurity in the commercial alloys and leads to a wide variety of Fe-containing intermetallics [7–9]. The relative volume fraction, chemical composition and morphology of these structural constituents have a deep impact on the material properties.

Among the other 6xxx alloys, the 6082 alloy stands out due to its combination of higher mechanical properties, excellent corrosion resistance and good weldability [10,11]. However, the high strength of the 6082 alloy limits its formability and requires higher forces in forming operations. Hence, before forming some annealing steps at high or moderate temperatures are required to improve the material ductility. Nevertheless, in addition of being time and energy consuming, elevating temperature may induce deformation and modification of the final product geometry among other parameters.

Within the last decades, the properties of the 6082-T6 alloy have been extensively investigated in terms of microstructure evolution within thermo-mechanical processing [12–16], welding [17,18] as well as grain refinement associated to severe deformation [19–22]. However, there is few works carried out on the cold forging of this material [23–25].

Cold forming at room temperature is an alternative to these problems. Cold forging is a process suitable for manufacturing low-cost and high quality automotive components made in high strength aluminium alloys [23]. This method is peculiarly appropriate for parts with narrow geometrical tolerances, good concentricity, smooth surface finish and for near net shape products.

* Corresponding author. Tel.: +33 327511391; fax: +33 327511411.
E-mail addresses: jeremie.bouquerel@univ-lille1.fr (J. Bouquerel), bmdiawara@yahoo.fr (B. Diawara), andre.dubois@univ-valenciennes.fr (A. Dubois), mirentxu.dubar@univ-valenciennes.fr (M. Dubar), jean-bernard.vogt@univ-lille1.fr (J.-B. Vogt), denis.najjar@ec-lille.fr (D. Najjar).

http://dx.doi.org/10.1016/j.matdes.2014.12.005
0261-3069/

Forming processes are characterised with a wide range of strain and strain rates. The degree of plastic deformation near the surface in the forming process is crucial when determining the mechanical and microstructural features of the work-piece surface, because the degree of plastic deformation strongly affects the development of grain structure in recrystallization. In addition, most of material failures come from the outer layers of the work piece (wear, fatigue, fretting damage, corrosion etc.). These phenomena are all extremely sensitive to the structure and to the properties of the surface of the material [26]. The investigation of the local plastic strain distribution occurring during forming allows a clear understanding of the effects of the macroscopic plastic strain on the local plastic strain gradient. Moreover, understanding these effects will not only contribute to develop guidelines in controlling deformation parameters (macroscopic plastic strain and strain rate) during surface plastic deformation processes but also predict the microstructure changes induced by cold forming that play a crucial role for mechanical failure and wear of materials [10].

The aim of the present work is to understand the effect of cold forging on the microstructure changes of the 6082 aluminium alloy. Hence the laboratory developed Upsetting Sliding Test, which is able to reproduce a large variety of industrial forming processes, has been used. Here, the system focuses on conditions similar to those present in the vicinity of the blank holder during stamping or deep drawing process. The local strains have been estimated by FEM calculation prior to tests and their distribution were validated by means of advanced analysis tool such as Electron Back-Scatter Diffraction on a scanning electron microscopy (SEM-EBSD). The different process parameters, such as lubrication, penetration levels were investigated and some microstructure based criteria were adopted.

2. Experimental procedures

2.1. Cold forging testing

Cold forging tests are carried out on the Upsetting Sliding Test (UST) (Figs. 1 and 2), developed at TEMPO Laboratory in order to simulate physical and mechanical contact conditions of cold forging processes [27]. This testing stand allows simultaneous compression and translation movements. It is positioned on a classical servo-hydraulic tensile machine and it is composed of two parts: a moving part that is supported by a load cell and a fixed one integrated on the tensile machine. The contactor that represents the tool is arranged on the moving part, and the specimen that represents the workpiece is clamped on the fixed part. The cylindrical geometry of the specimen, used in previous works [27], has evolved to a plate structure and the fixed stand has been slightly modified to welcome this plate specimen. Although this test is mainly dedicated to tribological analyses [28,29], its abilities to apply high contact pressure and to generate high plastic strains make it an efficient device to simulate forging sequences, *keeping the advantages of a laboratory facility.*

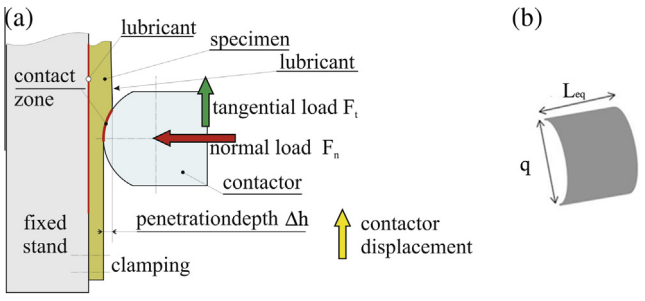

Fig. 1. (a) Schematic illustration and main parameters of the UST and (b) equivalent surface of contact.

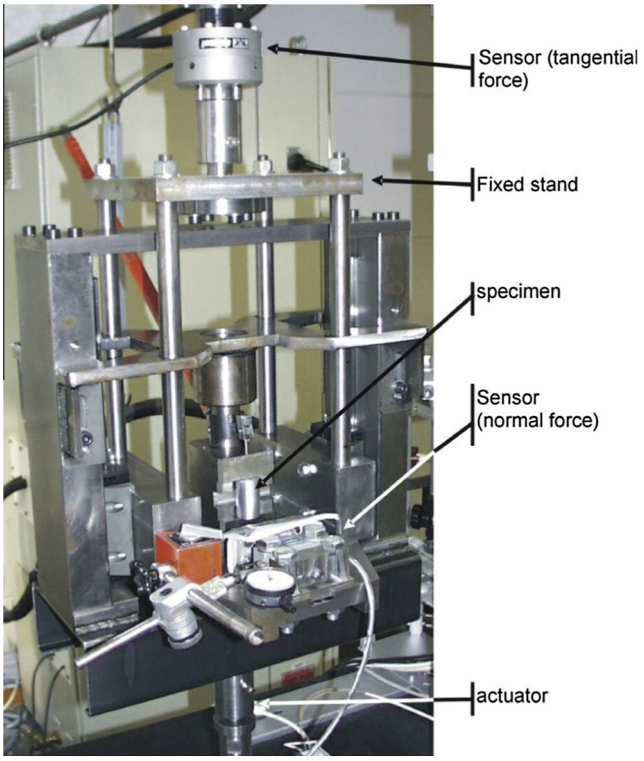

Fig. 2. Upsetting sliding test stand.

The principle of the test is rather simple and proceeds in two steps:

(1) Before the beginning of the test a relative penetration between the extremity of the contactor and the surface of the specimen is adjusted.
(2) The test starts and the contactor moves up towards the specimen. The contactor contacts the specimen and rubs straight on it, generating a locally deformed part.

Both normal (F_n) and tangential (F_t) forces are recorded during the test. Fig. 3 presents the typical evolution of the normal and tangential forces curves during the cold forging of the 6082 aluminium alloy. From these curves, it can be observed no contact occurs before 55 mm. This step is used to allow the increase of the contactor speed from zero to the desired value. As a consequence, when contact occurs, the contactor speed is constant, and remains constant until the end of the test. At a distance ranging from 55 mm to 65 mm the contactor enters in contact with the specimen, leading to an increase of the loads (zone A). Between 65 mm and 85 mm forces have a monotonic behaviour. This region (zone B) corresponds to the sliding area. Beyond 85 mm (zone C), the contactor starts leaving the contact and the forces abruptly decrease to zero.

The mechanical analysis of the upsetting sliding test leads to the mean normal contact pressure σ_n and to the mean tangential stress σ_t, as determined by the following equations [30]:

$$\sigma_n = \frac{F_t \Delta h + F_n q}{L_{eq}(q^2 + \Delta h^2)} \quad (1)$$

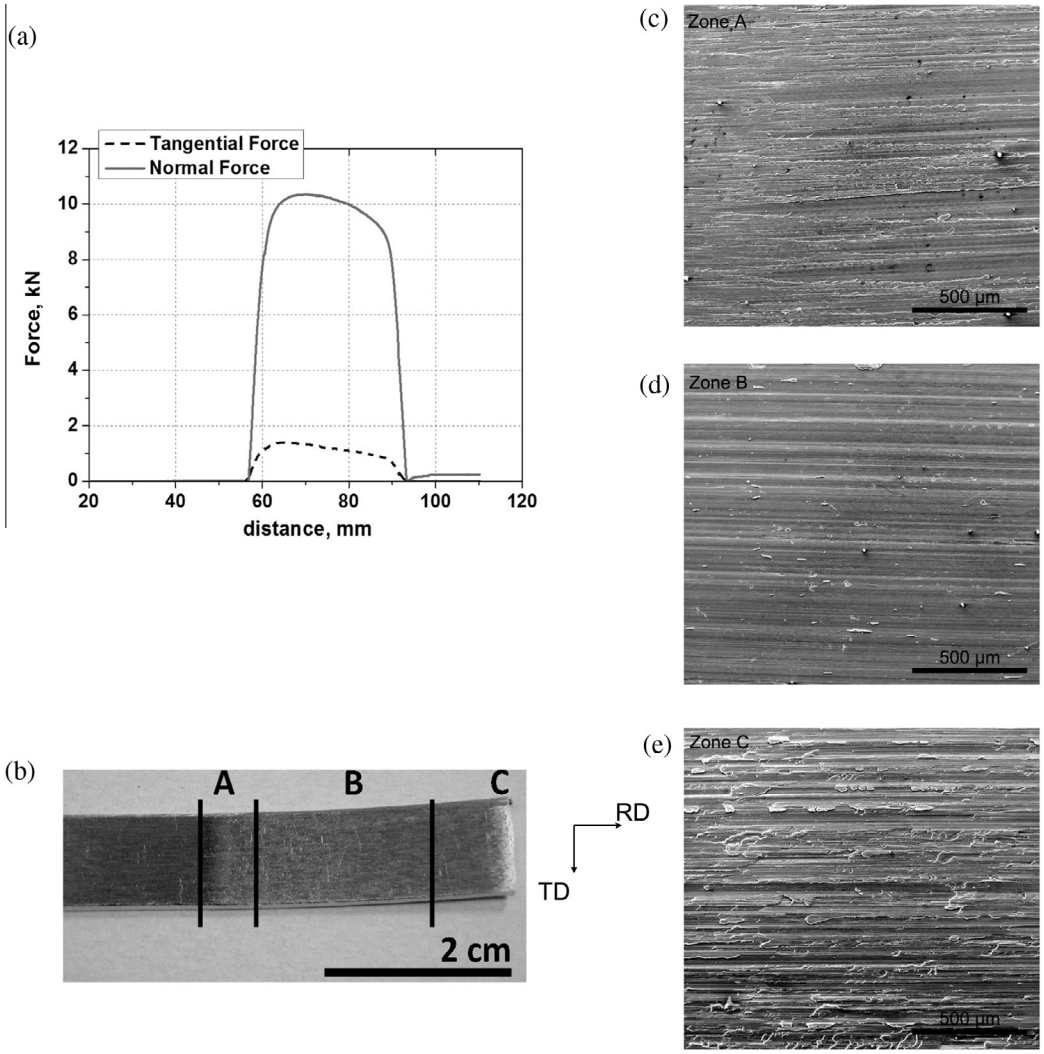

Fig. 3. Normal and tangential forces versus sliding distance during cold forging (a), localisation of the different areas on the specimen (b), and SEM micrographs of the surface after sliding (c–e).

$$\sigma_t = \frac{F_t q - F_n \Delta h}{L_{eq}(\Delta h^2 + q^2)} \tag{2}$$

where Δh, q and L_{eq} are respectively penetration depth, seating length and width of the contact surface (which corresponds to the width of the specimen). Finally, the mean Coulomb's friction coefficient μ can be expressed as follows:

$$\mu = \frac{\sigma t}{\sigma n} = \frac{q(F_t/F_n) - \Delta h}{\Delta h(F_t/F_n) + q} \tag{3}$$

As reported in Fig. 3, after 85 mm (zone C) the abrasions amount is relatively high. Then, for comparative observations only the surface of the zone B, for which the forces are almost constant, is considered.

In addition these "direct" results, finite element analyses of the tests are performed. These computations aim to quantify the effect of the penetration depth p on the effective plastic strain in the vicinity of the contact zone.

The UST is simulated using the ABAQUS Standard finite element software, version 6.12. Only the part of the specimen subjected to sliding is considered. The dimension of the model is then 2 mm × 30 mm. The specimen is modelled with 2D bilinear plane strain elements with full integration (CPE4 elements). The element size equals 0.1 mm. This leads to a total of 40 integration points distributed through the specimen thickness. The integration point closer to the contact zone is located at 0.02 mm beneath the surface. The strain–stress law associated to these elements is obtained from tensile tests.

Considering the large differences between specimens and tool steel hardness, the fixed stand and the contactor are modelled as rigid elements. The Coulomb's friction law is used to model friction. The coefficient of friction involved for each computation is identified from the experimental UST results according to Eq. (3).

2.2. Metallographic investigation

In order to have a clear understanding of the microstructure of the 6082-T6 alloy as well as its evolution within the various forging conditions, both EDS and EBSD analysis were carried out on a FEI Quanta 400 electron microscope fitted with an Oxford Instruments EDS/EBSD system.

EBSD specimens were prepared by grinding, polishing and a final mechanical–chemical vibratory polishing using colloidal suspension. A Nordlys CCD camera was used for pattern acquisition. Data were recorder at 300 nm step size using Oxford Instruments Aztec software. The analysis was carried out using both Oxford Instruments Channel 5 and TSL OIM 6 commercial software. By choosing the highest possible image resolution for pattern processing and by

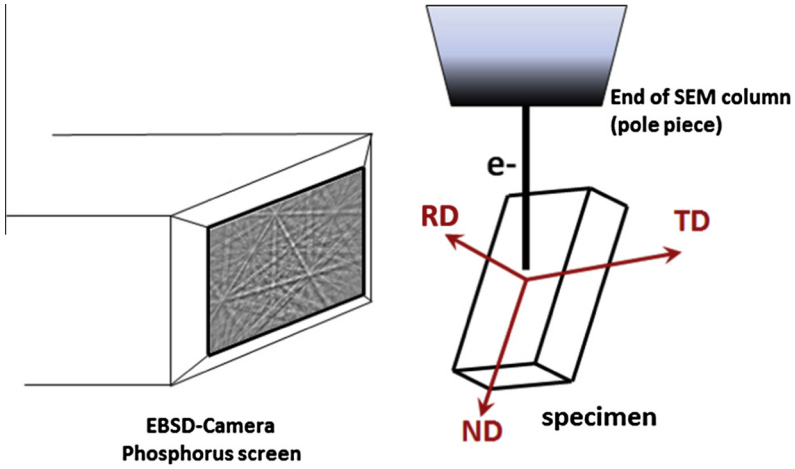

Fig. 4. Definition of directions in the EBSD analysis (case of the RD plane).

optimising the Hough transform parameters, an angular resolution of about 0.3° has been measured [31,32].

For the investigated specimens, the main observations were made on the edge and centre areas of the TD or ND surfaces oriented at an angle of 70° to the horizontal (see Fig. 4).

The EBSD analysis has been carried out in terms of Orientation Image Microscopy (OIM), which means that the orientations of the crystals have been only considered in this work. Then, using OIM analysis, the deformation of the 6082-T6 alloy was considered by two approaches: the Line Segment Method (LSM) and the study of misorientations trough the Kernel Average Misorientation (KAM), the Grain Orientation Spread (GOS) and the Grain Average Misorientation (GAM). The definition of the different parameters is given as follows.

The schematic illustration showing a grain composed of pixels in the EBSD measurement is shown in Fig. 4. The thick lines represent the grain boundaries determined as boundaries which have misorientation larger than 15°. Each pixel *i*, having a crystal orientation datum, has eight neighbouring pixels because the orientation mapping was done on a square grid.

In the first approach (LSM) [33,34] grain boundaries or more precisely grain boundary traces are represented by line segments separating adjacent EBSD points associated with specific misorientations ranges. Indeed, whereas conventional metallography considers a grain boundary as a line separating two grains, OIM grain boundary refers to a line segment separating two measurement points in a scan. Hence, three types of boundaries are generally considered: the High Angle Grain Boundaries (misorientations usually higher than 15°, which correspond to the metallographic "grain boundaries"), the Low-Angle Grain Boundaries are associated with misorientations between 2° and 15°, although some authors mention that the misorientations lower than 5° correspond to intragranular boundaries.

The second approach, based on the study of local variations in misorientations is known as a good indicator of strain in crystalline materials [33,35–37]. Several tools for characterising local misorientation are available and kernel based or grain based methods.

Indeed, local misorientation can be characterised using a misorientation kernel approach. For a given point the average misorientation of that point with all of its neighbours is calculated with the proviso that misorientations exceeding some tolerance value (*maximum misorientation*) are excluded from the averaging calculation. Hence, when considering the Kernel Average Misorientation (see Fig. 5), the local misorientation value assigned to the centre point (P_i) is the average of these misorientations as expressed by the following formula:

$$\mathrm{KAM}_{P_i} = \frac{1}{N}\sum_{j=1}^{N}\Delta\theta_{ij}, \quad \Delta\theta_{ij} < 5^\circ \tag{4}$$

where N is the number of surrounding pixels that exhibit a misorientation $\Delta\theta_{ij}$ lower than 5°.

Such an approach allows a quantitative evaluation of the small local plastic strain gradients which are intricately linked to orientation gradients as plastic deformation is physically associated with dislocation glide and crystal lattice rotation [38–40].

The recent works on this kind of analysis make a direct link between KAM and plastic strain stored energy as well as geometrically dislocations densities [41–43]. However, the EBSD measurements are currently not able to distinguish clearly the type of dislocations. Measuring the dislocations densities variation is also more relevant when considering the HR-KAM development [44,45]. Hence, the current work only considers the KAM criteria for accumulated plastic strain energy.

The KAM depends on some factors related to the measurement conditions, especially the grid step. One way to overcome that drawback is to use a KAM derivative over distance, which is less sensitive to measurement parameters and still contains some information about strain. Hence, in the present work, all the samples have been measured using the same conditions; therefore all the results given by standard KAM can be compared.

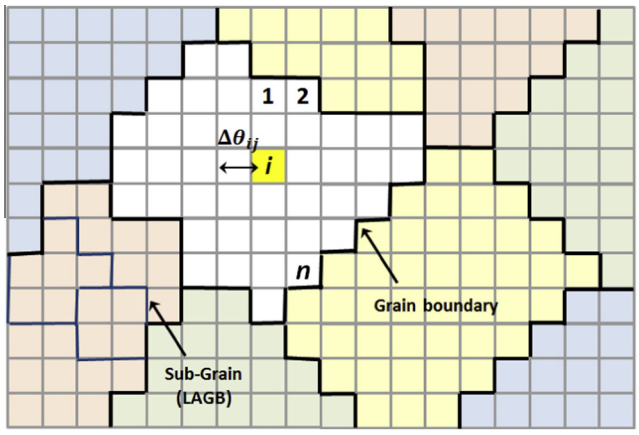

Fig. 5. Schematic illustration showing a grain composed of pixels in a square grid based EBSD measurement.

In addition, the grain based functions are helpful for identifying grains with varying local misorientation or the local orientation variations within a grain. In the case of Grain Average Misorientation, for a given grain, to each measurement point is associated the mean misorientation of all the pixels inside the grain. For the whole analysed area, the GAM parameter can be defined as follows:

$$\mathrm{GAM}_{\mathrm{Grain}} = \frac{1}{m}\sum_{j=1}^{m}\Delta\theta_{ij} \tag{5}$$

$$\mathrm{GAM}_{\mathrm{area}} = \frac{\left\{\sum_{k=1}^{G}\mathrm{GAM}_{\mathrm{grain}}A^{k}\right\}}{\sum_{k=1}^{G}A^{k}} \tag{6}$$

where m is the number of pixels inside a grain, G the number of grains included in the analysed area and A^k the area of a grain k.

In the last considered parameter, Grain Orientation Spread (GOS), to each measurement contained within the grain is assigned the same local misorientations value, but values differ from grain to grain. In this mode each point in the grain is shaded the same colour in maps of this type. The average orientation of the grain is calculated. The misorientation between this average orientation and the orientation of each individual measurement point within the grain is calculated. The average or these misorientations is then determined and assigned to each point within the grain.

Table 1
Design of experiments: UST main inputs.

Input data					
Penetration depth (μm)	30	60	90	120	240
Lubrication	MoS_2	MoS_2	MoS_2	MoS_2	Without lub.

$$\mathrm{GOS}_{\mathrm{grain}_\alpha} = \frac{1}{N-1}\frac{1}{N}\sum_{j=1}^{N}\sum_{i=1}^{N}\omega_j \tag{7}$$

The use of a unique EBSD criterion when determining the local plastic strain remains uncertain. Indeed, some authors report that both kind of material and loading type affect the choice of an EBSD parameter.

More interestingly, KAM/GAM and GOS approaches appear to be complementary since the first ones consider localised information of the strain, whereas the latter focuses on strain distribution gradients at a larger scale [34,46,47].

2.3. Design of experiments

In order to quantify the influence of cold forging on AA6082 microstructure, a set of five Upsetting-Sliding Tests is performed with penetration depth increasing from 30 to 240 μm. Molybdenum bisulfide lubricant is used to reduce friction at the interface, and to guaranty a low and steady coefficient of friction. Nonetheless, experiments with the penetration depth equals to 240 μm are conducted without lubricant to investigate the effect of large shear stress on the aluminium microstructure (Table 1).

3. Results and discussion

3.1. Characteristics of the as-received material

The studied material is a rolled 6082 aluminium alloy in the T6 condition. Its chemical composition is summarised in Table 2. The considered T6 treatment consists of solution annealing for 1 h at 530 °C, subsequent cooling in the water and artificial ageing at 175 °C for 10 h. The material used as a tool is a common tool steel grade X38CrMoV5-3 which composition is given in Table 2.

Table 2
Chemical composition of the as received work-piece material and tool steel.

Material	Chemical composition (wt.%)								
6082 Aluminium alloy-T6	Si	Fe	Cu	Mn	Mg	Cr	Ni	Zn	Al
	0.92	0.41	0.07	0.58	0.78	0.04	0.01	0.03	Bal.
X38CrMoV5-3	Fe	C	Cr	Mo	V	Mn	Si		
	Bal.	0.35–0.4	4.8–5.2	2.70–3.20	0.40–0.60	0.30–0.50	0.30–0.50	–	–

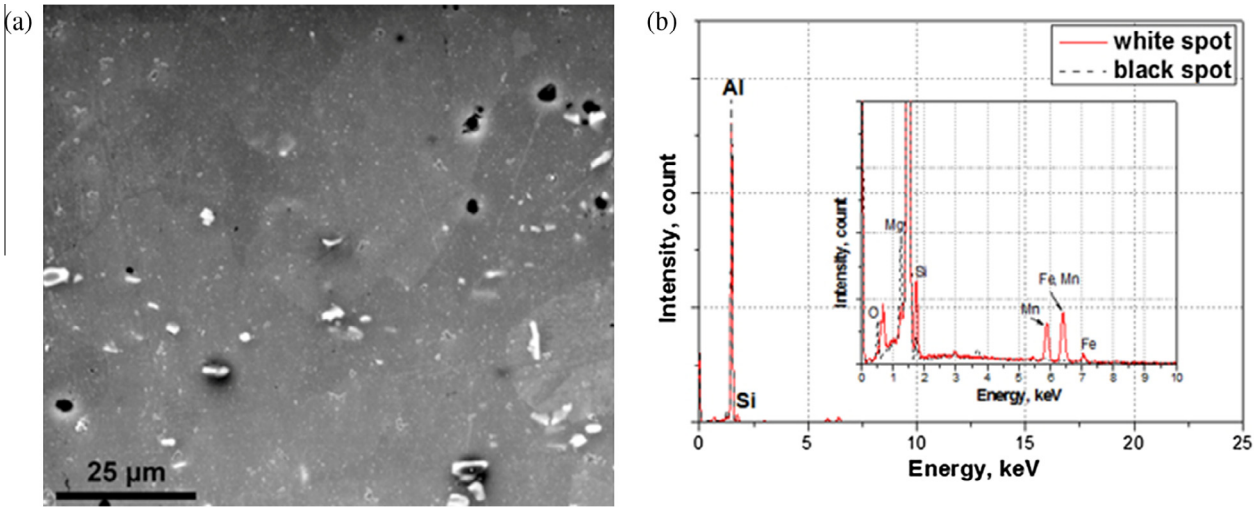

Fig. 6. SEM-BSE micrographs of the as-received 6082-T6 alloys (a) and EDS spectra of the white and black spots (b).

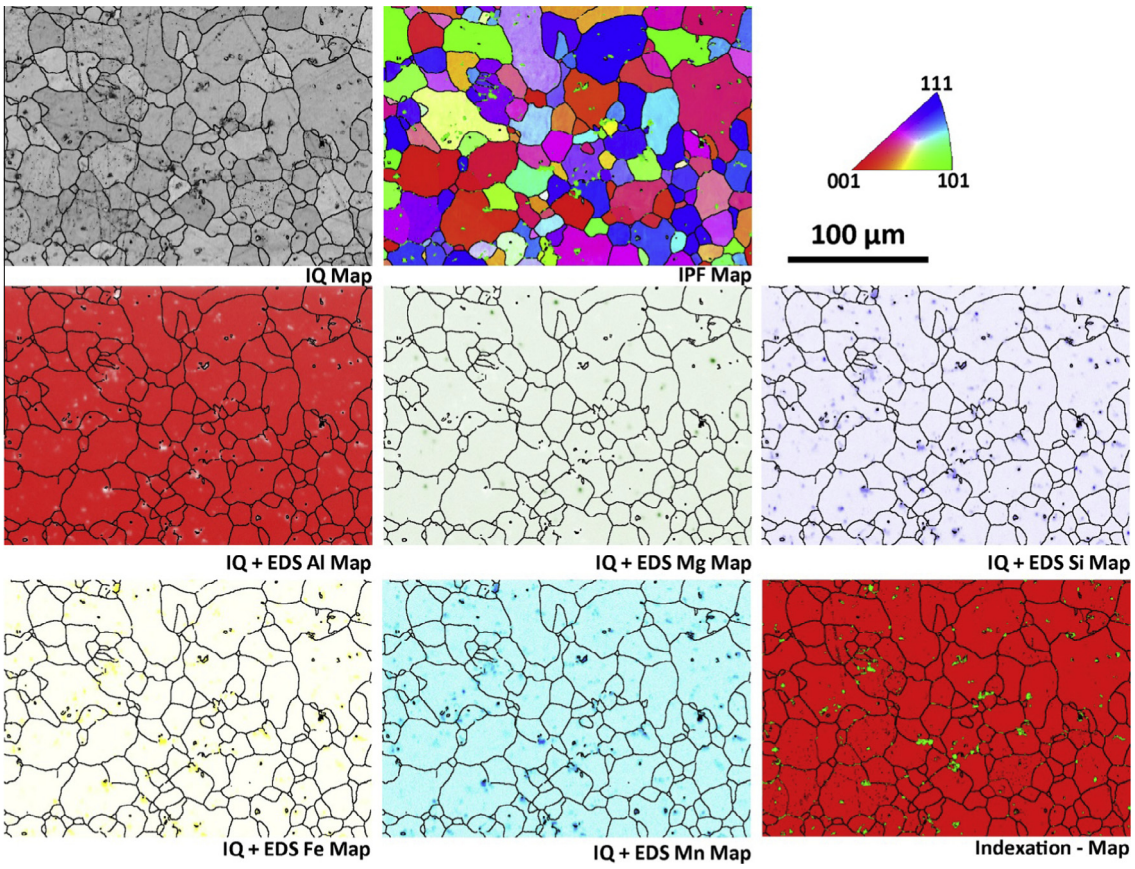

Fig. 7. Coupled EBSD–EDS analysis of the as received alloy (TD plane). (a) Image quality EBSD map, (b) inverse pole figure map and (c) EDS mapping showing the distribution of different constituting elements (Al, Mg, Si, Fe, Mn, O).

In order to limit the risk of material behaviour discrepancies and to minimise the effect of specimen machining on the residual stress state of the material, all the specimens involved in the present survey were machined by laser cutting from the same 2 mm thick sheet of aluminium.

Tensile tests have been performed in the two directions of the as received material. The tensile properties in the rolling direction (RD) are slightly higher than in the transverse direction (TD), but the differences remain lower than 2% and the material can be assumed as isotropic.

The bulk behaviour of the material is characterised according to the Ludwik's model. Ludwik's coefficients were identified from tensile tests performed on specimens machined in the rolling direction. Tests were performed with a crosshead speed displacement of 0.5 mm/s and longitudinal extensometer to accurately measure specimen elongations. For plastic strain in the range from 0 to 0.2, Ludwik's model is given by:

$$\sigma_0 = 272.43 + 289.35\varepsilon_p^{0.482} \tag{8}$$

Table 3
UST main mechanical results.

Penetration depth (µm)	30	60	90	120	240
Coefficient of friction μ (at position 70 mm)	0.058	0.043	0.038	0.052	0.542
Maximal plastic strain $\varepsilon_{ep\text{-}max}$	0.033	0.056	0.076	0.106	0.734
Mean plastic strain through the thickness ε_{ep}	0.022	0.044	0.064	0.091	0.268

where σ_0 is the bulk yield stress and ε_p is the equivalent plastic strain. The correlation coefficient between experiments and the model was slightly upper than 99%.

The as-received 6082-T6 alloys microstructure investigated with SEM-EDS and SEM-EBSD is shown in Fig. 6. The observed surface in SEM-BSE imaging (see Fig. 6a) shows a homogeneous matrix (M). A short EDS analysis (Fig. 6b) points out that Black spots (B) are either holes or intermetallic (second phase) precipitated particles containing mainly Mg (light element). White spot (W) are intermetallic constituent particles which concentrate all

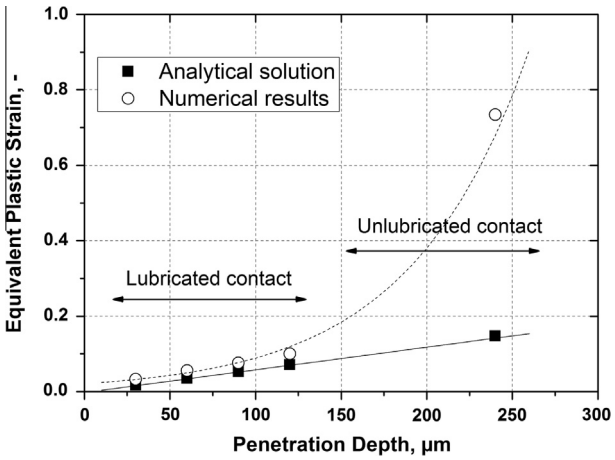

Fig. 8. Equivalent plastic strain versus penetration depth. Analytical predictions versus numerical computations.

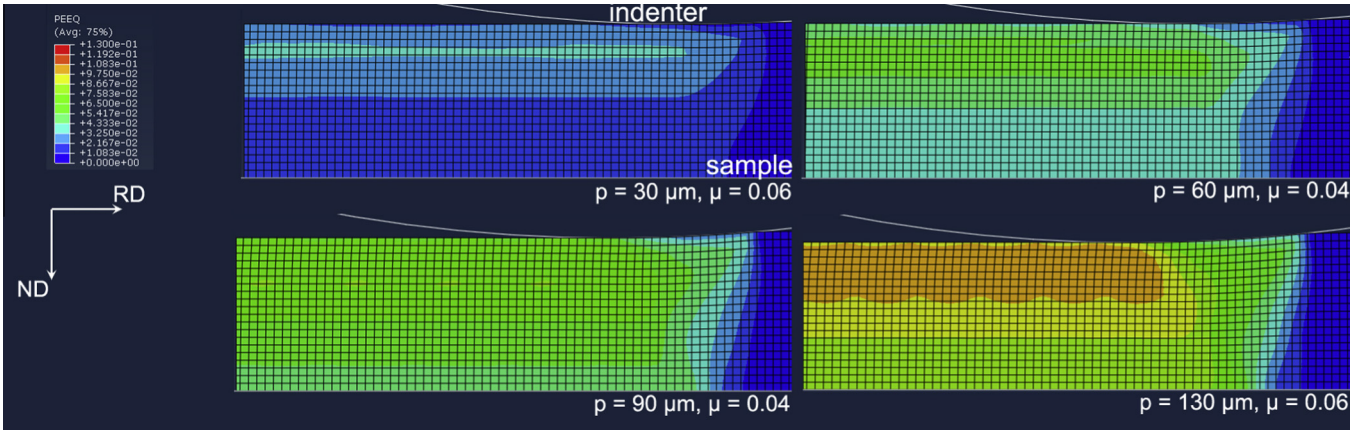

Fig. 9. Evaluation of the equivalent plastic strain levels and their localisation for four different penetrations (TD plane).

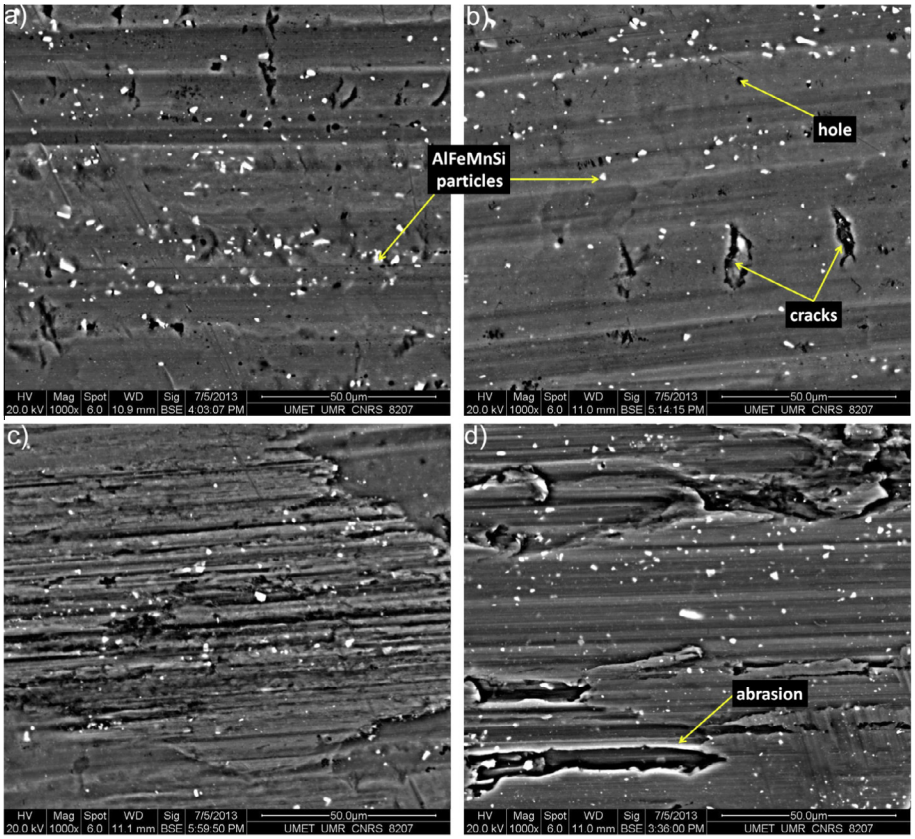

Fig. 10. SEM-BSE micrographs of 6082 aluminium alloy at different plastic strains: (a) unstrained, (b) lubricated and strained at 0.08, (c) lubricated and strained at 0.10 and (d) unlubricated.

the main second-phase elements except Mg (heavy elements, i.e. Fe, Mn and Cr). In addition, darker and brighter areas of the matrix may have identical chemical composition but different density of fine dispersed particles, as mentioned in other studies [48].

Those observations are consistent with the literature, which indicates that the 6082 alloys exhibits a large variety of intermetallic compounds ranging from Mg_2Si to $Al_xMn_yFe_zSi$ [5,6,49–52].

A complementary EBSD image quality (EBSD-IQ) map of the 6082 alloy in the as received condition is shown in Fig. 7. Here, each mapping point corresponds to the quality of an electron backscatter diffraction pattern. Lower IQ patterns correspond to a lattice distortion that can be related to structures such as grain boundaries, dislocation sub-structures [53–55]. The IQ map indicates that the material exhibits equiaxed grains with a mean grain size of 20 µm. In addition, the Inverse Pole Figure (IPF) map related to the loading direction confirms that the material does not present significant morphologic or crystallographic texture for the considered solicitations.

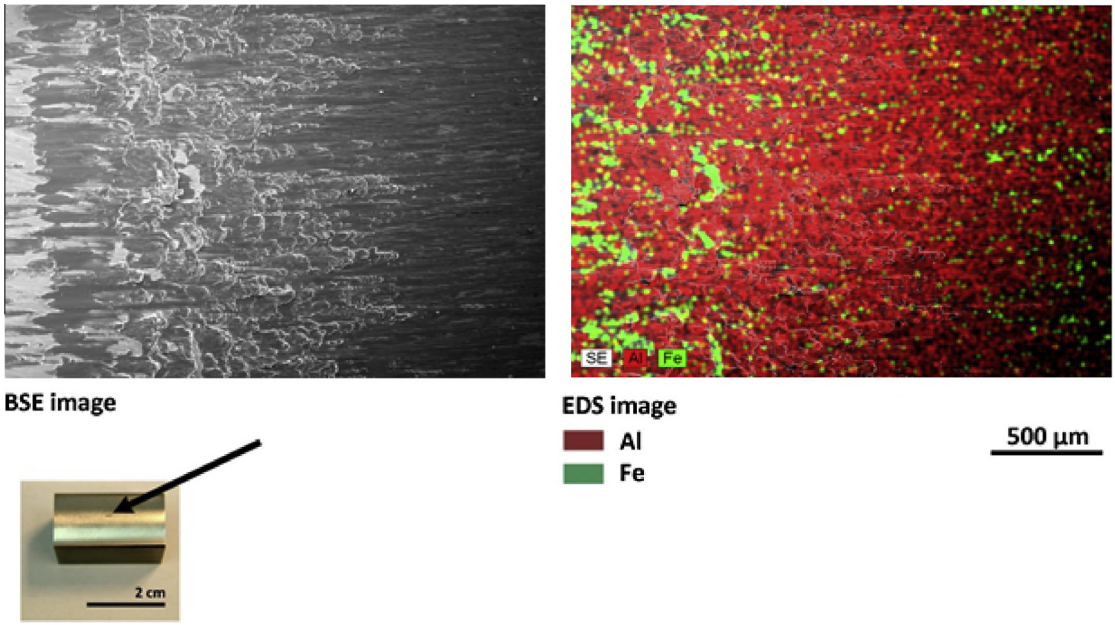

Fig. 11. SEM micrographs of the indenter surface after dry friction test: (a) SE-macro view and (b) EDS mapping of chemical elements.

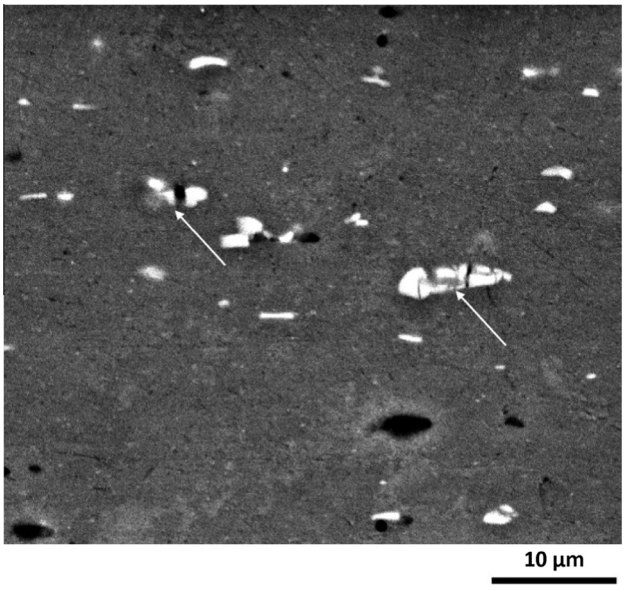

Fig. 12. SEM-BSE micrograph showing the aspect of the intermetallic particles after cold forging.

A coupled EBSD-EDS analysis points out that the brightest IQ-regions are rich in Al, Fe, Si and Mn and correspond to intermetallic particles (Fig. 7). The size of the intermetallic particles ranges from 1 µm to 10 µm. The dark spots (low IQ patterns) consist of holes and no other elements than aluminium and oxygen are detected. The intermetallic particles appear inside the matrix and in the vicinity of the grain boundaries.

3.2. Mechanical analyses and finite element results

FEM calculations have been carried out for the lubricated and unlubricated conditions in order to quantify the strain–stress state encountered by the 6082-T6 specimens. For each contact condition, experimental test have been performed, coefficients of friction have been identified from experimental forces according to relation (3) and used as friction input in the finite element models.

A thick solid film lubrication regime is encountered at the contactor/specimen interface when performing tests with MoS_2 lubricant. So for penetration depths increasing from 30 to 120 µm the Coulomb's coefficients of friction remain roughly constant at 0.048 ± 0.01. A limit lubrication regime is encountered for tests performed without lubricant. A significant increase of the coefficient of friction is then observed (Table 3).

The plastic deformation results from the upsetting of the specimen in one hand, and from the shear stress generated by friction in the other hand. When the specimen thickness e is 10 times larger than the penetration depth Δh, the equivalent plastic strain due to upsetting is assumed to be uniform and can be estimated by:

$$\varepsilon_{p\text{-upsetting}} = \frac{2}{\sqrt{3}} \ln\left(\frac{e}{e-\Delta h}\right) \approx \frac{2p}{e\sqrt{3}} \tag{9}$$

When friction occurs, the shear stress increases and implies an increase of the plastic strain. For tests performed with lubricant, the coefficient of friction is low and almost constant. So the friction stress does not have a strong influence on the plastic strain distribution. As a consequence the maximum of effective plastic strain increases linearly with the penetration p with a value slightly higher than the one predicted by Eq. (9). For tests performed without lubricant, the coefficient of friction is large and leads to high friction stresses. Thus the plastic strain strongly increases and the relation between the plastic strain and the penetration is no more linear (Fig. 8).

The distribution of the deformation is not uniform through the specimen thickness. Indeed, the deformation appears to be stronger a hundred of micrometres below the contact surface. In fact the highest values of equivalent plastic strains are located where the shear stresses reach maximum values [56]. The highest shear stress occurs at the point of greatest difference between the tensile or compression stresses in the (RD) and (TD) directions. As a consequence, the maximum of plastic strain is reached beneath the surface for lubricated tests while the maximum is reached at the surface for unlubricated tests (Fig. 9). These result is consistent with Ludema's work, based on Hertz theory, who showed that for a Coulomb's coefficient of friction greater than 0.3, the point of maximum shear stress between sliding bodies emerges to the surface [57].

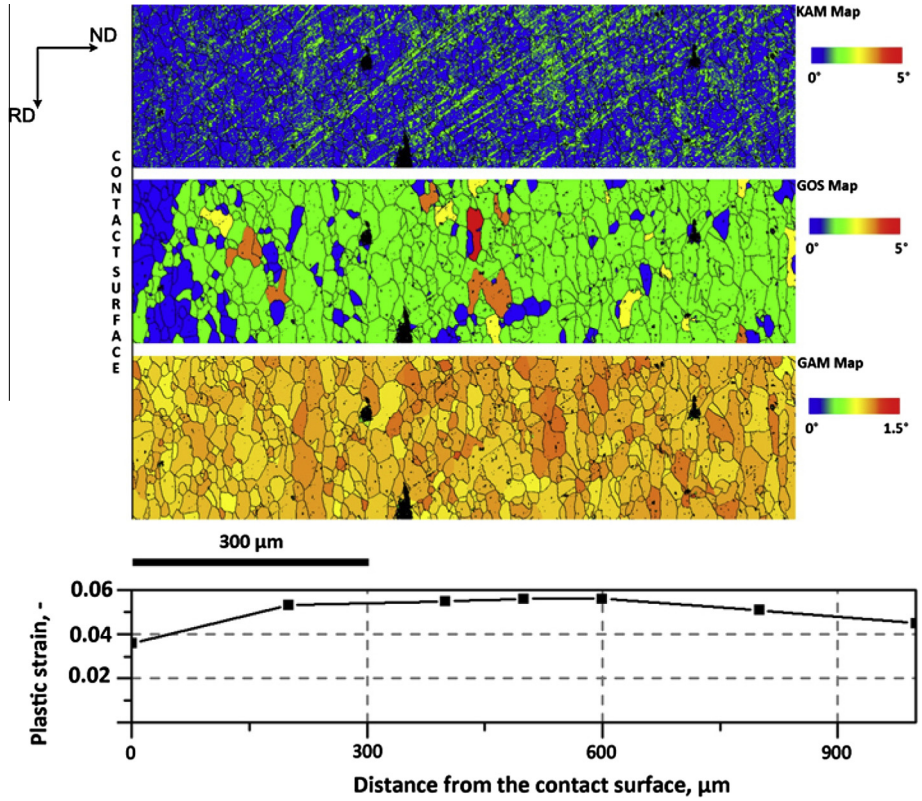

Fig. 13. TD cross-section of the 6082-T6 sample after an applied penetration of 60 µm ($\varepsilon = 0.06$) (colour coded OIM Maps: (a) KAM, (b) GOS and (c) GAM). Corresponding evolution of the mean plastic strain as a function of the depth issued from FEM calculations. (For interpretation of the references to colour in this figure legend, the reader is referred to the web version of this article.)

3.3. Characterisation of surface damage issued from the cold forging

The surface of the specimens prior and after sliding is shown in Fig. 10. All the presented SEM micrographs come from back-scattered electron signals and are related to the chemical composition. Fig. 10a shows that the surface of the specimen before testing is not homogeneous. It presents wide grooves in the longitudinal direction. This orthotropic surface is typical of a cold rolled surface where the grooves result from roughness transfer from the roll cylinder [58]. The surface of the specimen tested with a 30 µm penetration depth does not present significant differences with the initial specimen surface (Fig. 10b). The wide grooves generated by cold rolling are still present after testing and the initial cracks do not seem to open up. This observation is in good agreement with the finite element computations showing that the equivalent plastic strain at the surface of the specimen is almost null under this condition of contact (Fig. 9). For higher penetration depths, a strong plastic deformation and surface layers abrasion take place. The contactor asperities press strongly the surface layer of aluminium alloy leading to plastic deformation, localised cracking and to the formation of scratches (Fig. 10c).

A comparison of the surfaces properties has been made between lubricated and unlubricated specimens. It can be seen in Fig. 10 that the use of lubricant reduces the surface abrasion and scratches. In addition unlubricated specimens exhibit higher value of coefficient of friction than the lubricated ones (Table 3). This observation reflects the fact that friction on dry aluminium alloy surface causes a lot of adhesion of aluminium onto the contactor [59,60] to form hard Alumina particles (Al_2O_3). These ones latter contribute to the increase of the friction stress, of scratches and surface damage. The surface of the contactor after dry sliding is presented in Fig. 11, where the adhered aluminium elements are revealed by EDS analysis and appear in red[1] colour on the micrograph.

Table 4
Grain size and morphology evolution as a function of the cold process parameters.

	As received	Lubricated		
		Strain = 0.06	Strain = 0.08	Strain = 0.10
Mean grain diameter (µm)	20 ± 8	17 ± 8	15 ± 7	14 ± 8
Grain aspect ratio	0.49 ± 0.10	0.49 ± 0.13	0.53 ± 0.11	0.466 ± 0.124

3.4. Intermetallic particles behaviour during cold forging

The microstructure of the tested alloy exhibits the appearance of the hard brittle intermetallic precipitates fractured in the matrix (see Fig. 12). As observed, the elongated particles along the main loading direction break into several fragments depending of the particle length.

Holes are also found near the intermetallic particles. This suggests that intermetallic particles are pulled out during the cold forming. The dimple can then grow by plastic deformation until final coalescence [61]. These results are in agreement with the literature where it is reported that damage during forming can be initiated by decohesion or fracture of second phase particles. Moreover, the literature also reported that the mechanisms of decohesion are followed by the nucleation of voids at the interface between matrix and intermetallic α-$Al_x(FeMn)_ySi_z$ phase precipi-

[1] For interpretation of color in Figs. 11, 13 and 15, the reader is referred to the web version of this article.

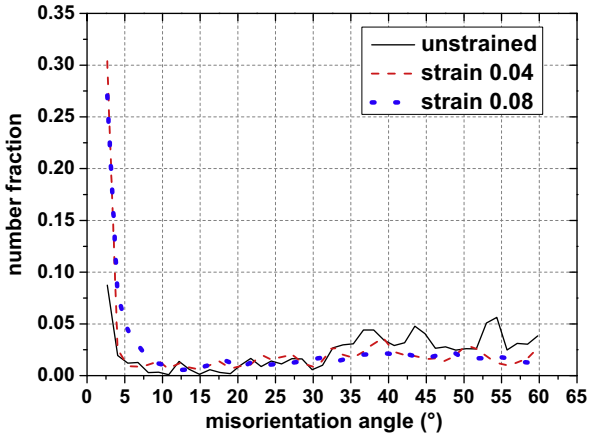

Fig. 14. Misorientation distribution of the as received and cold processed 6082-T6 alloy.

tates [5,62]. The resistance to damage and fracture depends partly on the nature, shape, distribution and volume fraction of the second phase particles. The plastic deformation resulted from the present cold forming conditions was efficient enough in affecting particles. This will have a direct effect on the formability such as reduced workability that leads to a poor surface finish.

During forming process, because of the interactions between constituent particles and dislocations, the particles structure could have a significant effect on the evolution of texture and microstructure in aluminium alloys [15].

3.5. Experimental estimation of the thickness of material affected by the process

SEM-EBSD analysis has been carried out on a LD-TD section in order to validate the FEM calculations. Several areas have been investigated close to the contact surface and in the bulk specimen. Fig. 13 shows the spatial distribution of the different misorientation parameters (KAM, GOS and GAM) by three colour coded maps for a specimen with a penetration of 60 μm. Although the GAM map does not show a strong variation within the distance from contact surface, KAM and GOS show a similar trend. Also note that the KAM values remain generally low but some grains exhibits a strong localisation of strain. Indeed, for the first 100 μm from the contact surface, both values are relatively low (blue areas). This corresponds to an area with low accumulated strain energy and also low strain heterogeneity.When comparing the experimental measurements (Fig. 13a–c) to the calculation (Fig. 13d), a good correlation can be established.

3.6. Influence of the cold forging parameters on the microstructure evolution

As shown previously, the whole material is deformed by the cold process although the layers close to the contact surface are less affected. After cold forging the reduction in term of grain size is not significant, with a change in aspect ratio value from 0.5 to 0.43 by increasing the plastic strain from 0 to 0.08 (Table 4). For strong levels of shear, such as in ECAP processing, the literature reports that aluminium and its alloys undergo grain refinement with increasing deformation [19,21,22,63]. In the current work the microstructure does not show any grain refinement. This is probably due to the fact that the applied plastic strain was not sufficient to lead to the grain refinement. In addition, contrary to the hot extrusion process that leads to recrystallization and duplex microstructure [64], the material keeps almost a constant microstructure, which means that the temperature increase during the test remained low.

Although no grain refinements or recrystallization phenomena are observed in the current work, the EBSD analysis performed on the forged specimens shows relevant changes of the microstruc-

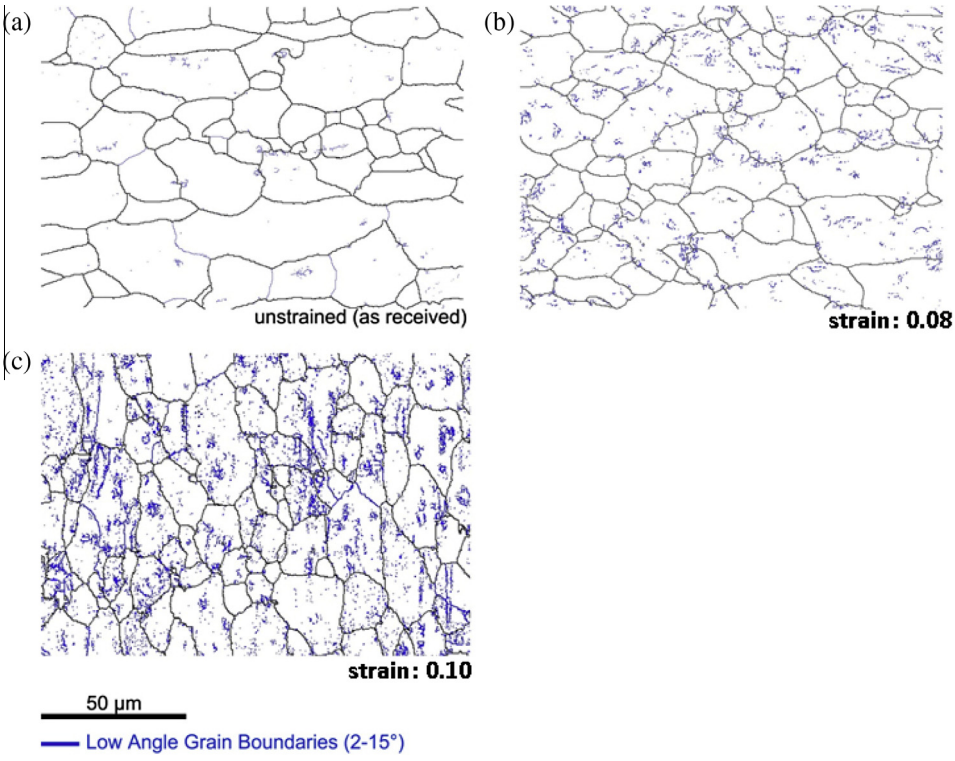

Fig. 15. Grain boundary maps of deformed material as a function of the nominal plastic strain level (a: 0, b: 0.06 and c: 0.08). Evolution of the grain boundaries density during cold deformation (d).

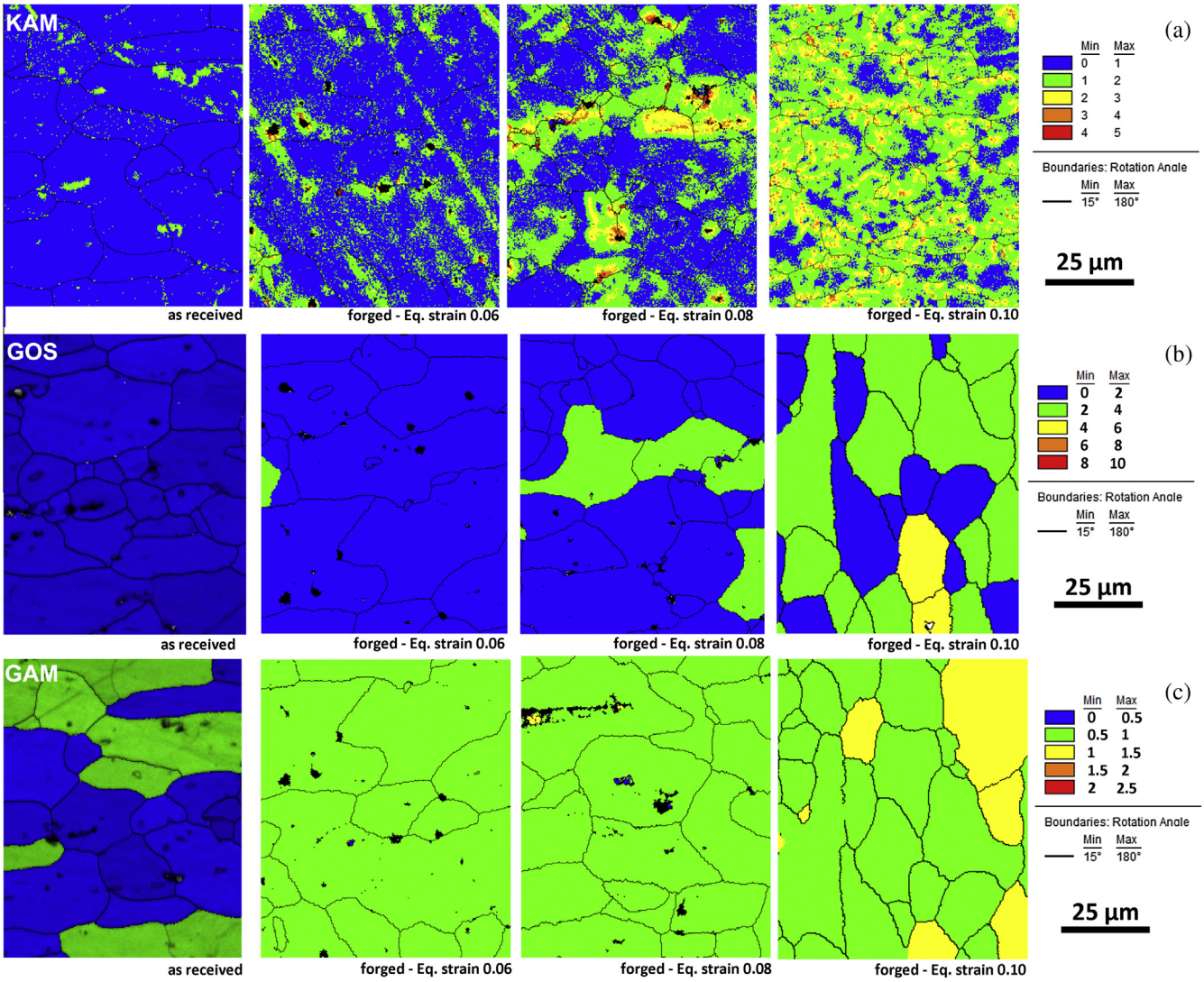

Fig. 16. Colour coded mapping – influence of the cold forging nominal strain: (a) Kernel Average Mapping (stored strain energy mapping), (b) Grain Orientation Spread and (c) Grain Average Misorientation (TD plane). (For interpretation of the references to colour in this figure legend, the reader is referred to the web version of this article.)

ture. In a first approach, the changes in term of misorientation angle distribution attest of a local strain levels (see Fig. 14). Indeed, the increase of nominal plastic strain results in a decrease of the fraction of high angle misorientation and an increase of low angle misorientation. This indicates that sliding promotes nucleation of new dislocations sub-structures.

Hence, in order to have a deeper comprehension on the microstructure evolution within cold forging, the LSM as well as misorientation based approaches have been carried out.

3.6.1. LSM approach

Fig. 15 illustrates the evolution of the grain boundaries maps as a function of the applied plastic strain. High Angle Grain Boundaries (HAGB) with misorientation up to 15° are plotted as solid black line and Low Angle Grain Boundaries (LAGB) with misorientation comprised between 2° and 15° are plotted as blue line.

The few LAGB identified in the unstrained microstructure are attributed to the presence of intermetallic particles. The formation of LAGBs is mainly observed for the deformed samples and their densities increase with magnitude of the plastic strain. Several authors have reported that intra-granular misorientations are indicative of dislocation structures which have accumulated during deformation [65]. Furthermore, aluminium and its alloys generally develop cell structures and sub-grains leading to the formation of finer grains after severe plastic deformation [14]. In the present work, the observed sub-structures do not lead to the formation of finer grains with high angle boundaries. This is due to the fact that during cold forging at small plastic deformation magnitude there is no migration of the grain boundaries and intermetallic particles act as obstacles against migration of grains.

3.6.2. Misorientation distribution approaches: KAM, GOS and GAM

Colour coded KAM maps of the tested specimens are shown in Fig. 16a. In respect to the as received material, lower KAM values are obtained. This explains the small amount of deformation for the as received state. As the nominal plastic strain increases, the KAM increases and is widespread inside the grains. Nevertheless, the largest orientation gradients are found in the vicinity of the grain boundaries, showing a localisation of the deformation in those areas. Note also that the areas surrounding the non-indexed black particles exhibit higher values of KAM. Here, decohesion or fracture of second phase particles can initiate extra-deformation within the Al–Mg–Si matrix. This observation confirms other results from the literature [61].

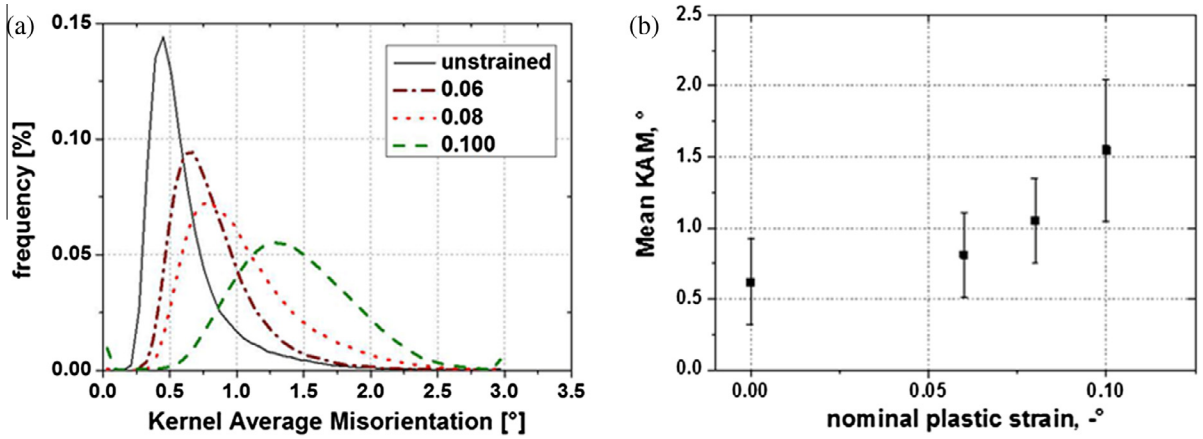

Fig. 17. Evolution of the KAM distribution as a function of the applied strain (a) statistical distribution and (b) averaged KAM values for the as-received and cold forged samples).

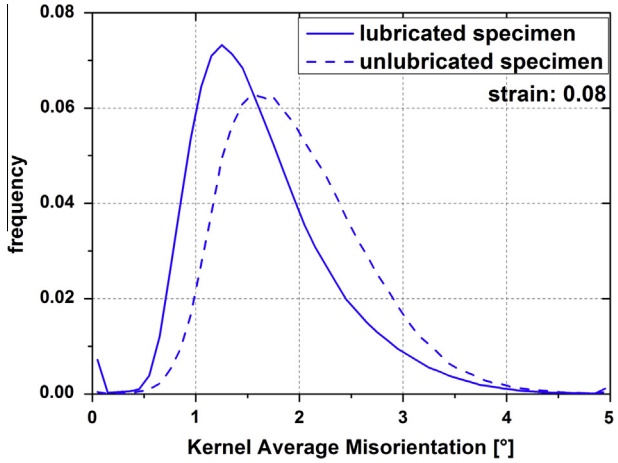

Fig. 18. Lubrication effect of the cold forging at 0.08 nominal plastic strain–KAM distribution.

Fig. 17a illustrates the distribution of KAM as a function of the macroscopic nominal strain. All the distributions exhibit nearly similar shape except for the as received specimen which has a log-normal distribution with an average KAM value of 0.62° indicating a small and randomly distributed local plastic strain, as reported by Zhong et al. [66].

Furthermore, the KAM distribution of the deformed specimens globally shows a shift to the higher values and provides a large dispersion which corresponds to the widespread of the misorientation. In addition, the mean KAM value increases with the magnitude of the nominal plastic strain (Fig. 17b). Nevertheless, a non-linear correlation is observed, whereas literature mainly reports that KAM varies almost linearly with the plastic strain.

The lubrication effect on the cold forming is also observed. Indeed, KAM values of the unlubricated specimens are higher than those of the lubricated ones (Fig. 18). This is likely due to the fact that lubrication reduces the friction of the indenter on the specimen and so local surface strengthening of the specimen.

In a same manner, the evolution of both GOS and GAM criteria has been investigated (Fig. 16b and c). The GOS maps do no show a clear evolution of microstructure for the lower penetration (equivalent plastic strain below 10%). This attests that the different grains do not present high levels of internal strain heterogeneity. For the higher penetration, the GOS levels of the grains increase of few degrees indicating that the amount of heterogeneities (such as the formation of dislocations sub-structures) increases. Nevertheless, it can be observed that some grains remain almost free of heterogeneities. This can be associated to the interaction between the matrix and the second phase particles. In the case of the GAM parameter that deals of the mean misorientation of the grains, it can be observed that the material exhibits a homogeneous evolution for the lowest penetration. For the higher one, the GAM remains relatively low but some grains are more misoriented. Regarding the few informations given by the GOS and GAM maps,

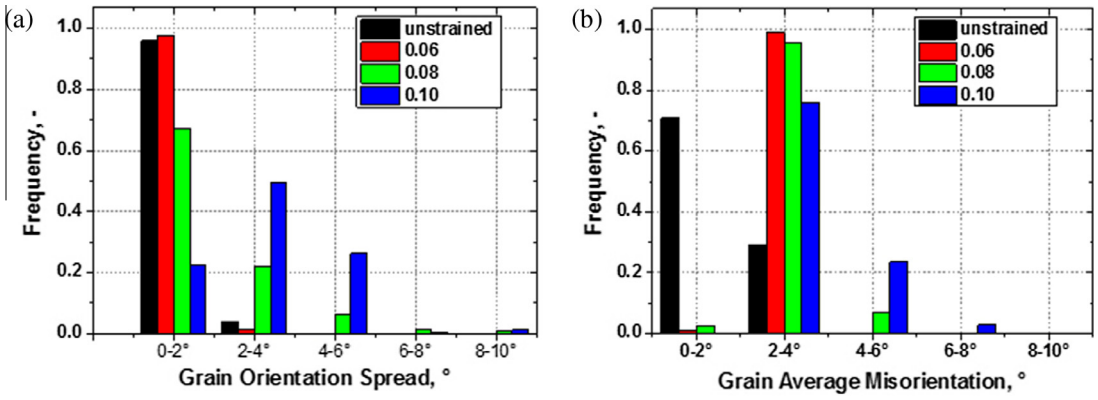

Fig. 19. Evolution of the GOS and GAM parameters as a function of the applied strain (statistical distribution).

the statistical distribution of those parameters have been investigated (Fig. 19). The values of both parameters shift to higher values as the applied strain levels increase. The major changes in term of GOS occur for the highest penetration (i.e. when the applied plastic strain equals 0.10).

Considering these misorientation approaches it appears that only the KAM and GOS give an interesting description of the microstructure evolution. Moreover, by coupling the KAM and GOS approaches the non-linear KAM-ε_p correlation proposed earlier can be divided in two linear correlations depending of the penetration. Indeed, two domains co-exist: for the lower penetrations (i.e. $\varepsilon_p < 0.75$) the internal strain heterogeneities (KAM values) are relatively low affected by the imposed penetration. By contrast, for the higher penetrations ($\varepsilon_p > 0.75$), the KAM is very sensitive to the imposed penetration. This can be related to the development and rearrangements of the dislocations structures.

The examination of those parameters also reveals a particular aspect since literature reports that large plastic deformations induce high modifications of the workpiece shape [67]. Hence, assessing the local strain through the EBSD-based criteria and FEM calculation prevents from any deformation of the workpiece.

4. Conclusions

The current work describes the microstructure changes of 6082 aluminium alloy during a cold forging process simulated by Upsetting Sliding Test, at different magnitudes of plastic strain. The microstructural evolution of the material was estimated by FEM calculation and SEM-EBSD observations. These characterizations showed a strong dependency of the local microstructure changes on the process parameters. The penetration increase induces an increase of the local strain levels as attested by the variations of the local misorientation inside the grains.

The lubrication effect on the cold forging was also studied. Here, the use of bisulfide molybdenum as lubricant was effective to reduce surface damage and the coefficient of friction. The main surface damages which were observed in the 6082 aluminium alloy were cracks, abrasion, holes, broken particles and plastic deformation. The observation of intermetallic particles near the holes was the evidence that intermetallic particles were removed from their location during plastic deformation.

When considering unlubricated conditions, a strong galling phenomenon exists. In that way, the FEM calculations that are based on the thickness measurements of the samples after testing may over-estimate the real strains encountered by the material. However, SEM-EBSD observations confirm a higher level of deformation in the unlubricated state.

For the lubricated conditions, the applied penetration and then the applied plastic strain do not affect the grain size itself but induce the development of sub-structures. Indeed, the observation of new low angle grain boundaries is an indication of the formation of dislocations structures during cold forging. This may lead to the hardening of the structure during forging.

SEM-EBSD appears here as an appropriate observation tool to reveal the micro-mechanisms of degradation and damage during forming process. It also allows the quantification of microstructural factor affecting the forging damage. Among the different criteria available when describing the plastic accommodation by the microstructure, KAM and GOS are the most suitable in order to develop indicators on the real local strains.

Acknowledgements

The present research work has been supported by International Campus on Safety and Intermodality in Transportation (CISIT), the Nord-Pas-de-Calais Region, the European Community, the Regional Delegation for Research and Technology, the Ministry of Higher Education and Research, and the National Center for Scientific Research. The authors gratefully acknowledge the support of these institutions.

References

[1] Davies G. Materials for automotive bodies. 2nd ed.; 2012.
[2] Jeswiet J, Geiger M, Engel U, Kleiner M, Schikorra M, Duflou J, et al. Metal forming progress since 2000. CIRP J Manuf Sci Technol 2000;1(2008):2–17.
[3] Karabay S, Yilmaz M, Zeren M. Investigation of extrusion ratio effect on mechanical behaviour of extruded alloy AA-6101 from the billets homogenised-rapid quenched and as-cast conditions. J Mater Process Technol 2005;160:138–47.
[4] Sieniawski J, Wierzbiñska M. Intermetallic phase particles in 6082 aluminium alloy. Arch Mater Sci Eng 2007;28:69–76.
[5] Mrówka-Nowotnik G, Sieniawski J, Wierzbińska M. Analysis of intermetallic particles in AlSi1MgMn aluminium alloy. J Achiev Mater Manuf Eng 2007;20:7–8.
[6] Mrówka-Nowotnik G, Sieniawski J. Influence of heat treatment on the microstructure and mechanical properties of 6005 and 6082 aluminium alloys. J Mater Process Technol 2005;162–163:367–72.
[7] Warmuzek M, Mrówka G, Sieniawski J. Influence of the heat treatment on the precipitation of the intermetallic phases in commercial AlMn1FeSi alloy. J Mater Process Technol 2004;157–158:624–32.
[8] Siddiqui RA, Abdullah HA, Al-Belushi KR. Influence of aging parameters on the mechanical properties of 6063 aluminium alloy. J Mater Process Technol 2000;102:234–40.
[9] Sha G, O'Reilly K, Cantor B, Worth J, Hamerton R. Growth related metastable phase selection in a 6xxx series wrought Al alloy. Mater Sci Eng A 2001;304–306:612–6.
[10] Geoffroy N, Vittecoq E, Birr a, de Mestral F, Martin J-M. Fatigue behaviour of an arc welded Al–Si–Mg alloy. Scr Mater 2007;57:349–52.
[11] Tveiten B, Fjeldstad A, Harkegard G, Myhr O, Bjorneklett B. Fatigue life enhancement of aluminium joints through mechanical and thermal prestressing. Int J Fatigue 2006;28:1667–76.
[12] Wang L, Zhou J, Duszczyk J, Katgerman L. Friction in aluminium extrusion—Part 1: a review of friction testing techniques for aluminium extrusion. Tribol Int 2012;56:89–98.
[13] Reiso O. Extrusion of AlMgSi alloys. Mater Forum 2004;28:32–46.
[14] Khan ZA, Chakkingal U, Venugopal P. Analysis of forming loads, microstructure development and mechanical property evolution during equal channel angular extrusion of a commercial grade aluminum alloy. J Mater Process Technol 2003;135:59–67.
[15] Zeng Q, Wen X, Zhai T. Texture evolution rate in continuous cast AA5052 aluminum alloy during single pass hot rolling. Mater Sci Eng A 2008;476:290–300.
[16] Hurley PJ, Humphreys FJ. The application of EBSD to the study of substructural development in a cold rolled single-phase aluminium alloy. Acta Mater 2003;51:1087–102.
[17] Costa JD, Ferreira JAM, Borrego LP. Fatigue behaviour of AA6082-T6 aluminium alloy friction stir welds under variable amplitude loading (n.d.).
[18] Moreira PMGP, Santos T, Tavares SMO, Richter-Trummer V, Vilaça P, de Castro PMST. Mechanical and metallurgical characterization of friction stir welding joints of AA6061-T6 with AA6082-T6. Mater Des 2009;30:180–7.
[19] Dadbakhsh S, Karimi Taheri a, Smith CW. Strengthening study on 6082 Al alloy after combination of aging treatment and ECAP process. Mater Sci Eng A 2010;527:4758–66.
[20] Angella G, Bassani P, Tuissi A, Vedani M. Intermetallic particle evolution during ECAP processing of a 6082 alloy. Mater Trans 2004;45:2182–6.
[21] Vedani M, Bassani P, Cabibbo M, Latini V, Evangelista E. Channel angular pressing O. A commercial AA6082 alloy. Metall Sci Technol 2003;21:2–9.
[22] Angella G, Dellasega D, Farè S, Vedani M. A comparison between asymmetric rolling and accumulative roll bonding as means to refine the grain structure of an Al–Mg–Si alloy. Metall Sci Technol 2010;28:22–6.
[23] Jensrud O, Pedersen K. Cold forging of high strength aluminum alloys and the development of new thermomechanical processing. J Mater Process Technol 1998;80–81:156–60.
[24] Sheljaskov S. Current level of development of warm forging technology. J Mater Process Technol 1994;46:3–18.
[25] Hirscvogel M, Dommelen Hv. Some applications of cold and warm forging. J Mater Process Technol 1992;35:343–56.
[26] Zhang X, Matsuura K, Ohno M, Suzuki S. Quantification of local plastic strain distribution beneath surface of deformed iron. Mater Sci Eng A 2013;564:169–75.
[27] Dubar L, Dubois A, Dubar M. Friction and wear phenomena in cold metal forming: an integrated approach. Proc Inst Mech Eng Part B J Eng Manuf 2006;220:1–10.
[28] Lazzarotto L, Dubois A, Dubar L, Verleene A, Oudin J. Testing of zinc phosphate/stearate coating according to true conditions of contact in wire drawing. Surf Eng 1998;14:335–8.

[29] Daouben E, Dubois A, Dubar M, Dubar L, Deltombe R, Truong Dinh NG, et al. Effects of lubricant and lubrication parameters on friction during hot steel forging. Int J Mater Form 2008;1:1223–6.
[30] Lazzarotto L, Dubar L, Dubois A, Ravassard P, Oudin J. Identification of Coulomb's friction coefficient in real contact conditions applied to a wire drawing process. Wear 1997;211:54–63.
[31] Dingley D. Progressive steps in the development of electron backscatter. J Microsc 2004;213:214–24.
[32] Bate PS, Knutsen RD, Brough I, Humphreys FJ. The characterization of low-angle boundaries by EBSD. J Microsc 2005;220:36–46.
[33] EDAX/TSL. OIM Analysis 7.0 Software User Manual; 2013. (UT) USA: EDAX/TSL.
[34] Jedrychowski M, Tarasiuk J, Bacroix B, Wronski S. Electron backscatter diffraction investigation of local misorientations and orientation gradients in connection with evolution of grain boundary structures in deformed and annealed zirconium. A new approach in grain boundary analysis. J Appl Crystallogr 2013;46:483–92.
[35] Kamaya M, Da Fonseca JQ, Li LM, Preuss M. Local plastic strain measurement by EBSD. Appl. Mech. Mater. 2007;7–8:173–9.
[36] Kamaya M, Wilkinson AJ, Titchmarsh JM. Measurement of plastic strain of polycrystalline material by electron backscatter diffraction. Nucl Eng Des 2005;235:713–25.
[37] Yoda R, Yokomaku T, Tsuji N. Plastic deformation and creep damage evaluations of type 316 austenitic stainless steels by EBSD. Mater Charact 2010;61:913–22.
[38] Godfrey A, Cao WQ, Liu Q, Hansen N. Stored energy, microstructure, and flow stress of deformed metals. Metall Mater Trans A 2005;36:2371–8.
[39] Bernd-Arno B, Hans C, Pavel P. Effect of temperature and strain rate on friction factor during microforming of AW-6082 AL-alloy. Int J Mater Form 2009;2:613–6.
[40] Vogt J-B, Bouquerel J, Léaux F, Palleschi F. Fatigue damage assessment of alternator fans by EBSD. Proc Eng 2013;66:608–14.
[41] Merriman CC, Field DP, Trivedi P. Orientation dependence of dislocation structure evolution during cold rolling of aluminum. Mater Sci Eng A 2008;494:28–35.
[42] Field DP, Merriman CC, Allain-Bonasso N, Wagner F. Quantification of dislocation structure heterogeneity in deformed polycrystals by EBSD. Model Simul Mater Sci Eng 2012;20:024007.
[43] Pantleon W. Resolving the geometrically necessary dislocation content by conventional electron backscattering diffraction. Scr Mater 2008;58:994–7.
[44] Ben Britton T, Jiang J, Karamched PS, Wilkinson AJ. Probing deformation and revealing microstructural mechanisms with cross-correlation-based, high-resolution electron backscatter diffraction. JOM 2013;65:1245–53.
[45] Jiang J, Britton TB, Wilkinson AJ. Measurement of geometrically necessary dislocation density with high resolution electron backscatter diffraction: effects of detector binning and step size. Ultramicroscopy 2013;125:1–9.
[46] Kamaya M. Assessment of local deformation using EBSD: quantification of local damage at grain boundaries. Mater Charact 2012;66:56–67.
[47] Zaafarani N, Raabe D, Roters F, Zaefferer S. On the origin of deformation-induced rotation patterns below nanoindents. Acta Mater 2008;56:31–42.
[48] Jíša D, Liškutín P, Kruml T, Polák J. Small fatigue crack growth in aluminium alloy EN-AW 6082/T6. Int J Fatigue 2010;32:1913–20.
[49] Mrówka-Nowotnik G. Intermetallic phase identification on the cast and heat treated 6082 aluminium alloy. In: Automn sch. mater. sci. electron microsc.; 2007. p. 5–6.
[50] Mrówka-Nowotnik G. Influence of chemical composition variation and heat treatment on microstructure and mechanical properties of 6xxx alloys. Arch Mater Sci Eng 2010;46:6–13.
[51] Zvinys J, Kandrotaite Janutiene R, Meskys J, Juzenas K. Investigation of thermo mechanical effect on structure and properties of aluminium alloy 6082. Int Virtual J Sci Tech Innov Ind 2012:3–6.
[52] Decroly A, Petitjean J-P. Study of the deposition of cerium oxide by conversion on to aluminium alloys. Surf Coat Technol 2005;194:1–9.
[53] Petrov RH, Bouquerel J, Verbeken K, Kestens LAI, Verleysen P, Houbaert Y. OIM analysis of microstructure and texture of a TRIP assisted steel after static and dynamic deformation. Mater Sci Forum 2010;638–642:3447–52.
[54] Wright SI, Nowell MM. EBSD image quality mapping. Microsc Microanal 2006;12:72–84.
[55] Wright SI, Nowell MM, Field DP. A review of strain analysis using electron backscatter diffraction. Microsc Microanal 2011;17:316–29.
[56] Goryacheva IG. Contact mechanics in tribology; 1998 <http://books.google.fr/books/about/Contact_Mechanics_in_Tribology.html?id=o8NHiF9WYYwC&pgis=1> [accessed 30.06.14].
[57] Ludema KC. Friction, wear, lubrication: a textbook in tribology (Google eBook). CRC Press; 1996 <http://books.google.com/books?id=YTi6CUI9Wa0C&pgis=1> [accessed 30.06.14].
[58] Le H, Sutcliffe MP. Analysis of surface roughness of cold-rolled aluminium foil. Wear. 2000;244:71–8.
[59] Pujante J, Pelcastre L, Vilaseca M, Casellas D, Prakash B. Investigations into wear and galling mechanism of aluminium alloy-tool steel tribopair at different temperatures. Wear 2013;308:193–8.
[60] Heinrichs J, Jacobson S. The influence from shape and size of tool surface defects on the occurrence of galling in cold forming of aluminium. Wear 2011;271:2517–24.
[61] Lassance D, Fabregue D, Delannay F, Pardoen T. Micromechanics of room and high temperature fracture in 6xxx Al alloys. Prog Mater Sci 2007;52:62–129.
[62] Mrówka-Nowotnik G. Damage mechanism in AlSi1MgMn alloy. Arch Mater Sci Eng 2008;29:93–6.
[63] Lampke T, Dietrich D, Nickel D, Bergmann M, Zachäus R, Neugebauer R. Controlled grain size distribution and refinement of an EN AW-6082 aluminium alloy. Int J Mater Res 2011;102:977–81.
[64] Poletti C, Rodriguez-Hortalá M, Hauser M, Sommitsch C. Microstructure development in hot deformed AA6082. Mater Sci Eng A 2011;528:2423–30.
[65] Ben Britton T, Birosca S, Preuss M, Wilkinson AJ. Electron backscatter diffraction study of dislocation content of a macrozone in hot-rolled Ti–6Al–4V alloy. Scr Mater 2010;62:639–42.
[66] Zhong Y, Yin F, Sakaguchi T, Nagai K, Yang K. Dislocation structure evolution and characterization in the compression deformed Mn–Cu alloy. Acta Mater 2007;55:2747–56.
[67] Groche P, Müller C, Stahlmann J, Zang S. Mechanical conditions in bulk metal forming tribometers—Part one. Tribol Int 2013;62:223–31.